Radio Activity of Supermassive Black Holes with Extremely High Accretion Rates

N.B. When citing this work, cite the original published paper.

(article starts on next page)

Radio Activity of Supermassive Black Holes with Extremely High Accretion Rates

Xiaolong Yang[1,2] , Su Yao[1,3] , Jun Yang[2,4] , Luis C. Ho[1,5] , Tao An[2] , Ran Wang[1,5] , Willem A. Baan[6,7] ,
Minfeng Gu[8] , Xiang Liu[6], Xiaofeng Yang[6], and Ravi Joshi[1]

[1] Kavli Institute for Astronomy and Astrophysics, Peking University, Beijing 100871, People's Republic of China; yxl.astro@gmail.com
[2] Shanghai Astronomical Observatory, Key Laboratory of Radio Astronomy, Chinese Academy of Sciences, 200030 Shanghai, People's Republic of China
[3] National Astronomical Observatories, Chinese Academy of Sciences, Beijing 100012, People's Republic of China
[4] Department of Space, Earth and Environment, Chalmers University of Technology, Onsala Space Observatory, SE-439 92 Onsala, Sweden
[5] Department of Astronomy, School of Physics, Peking University, Beijing 100871, People's Republic of China
[6] Xinjiang Astronomical Observatory, Key Laboratory of Radio Astronomy, Chinese Academy of Sciences, 150 Science 1-Street, 830011 Urumqi, People's Republic
of China
[7] Netherlands Institute for Radio Astronomy ASTRON, NL-7991 PD Dwingeloo, The Netherlands
[8] Key Laboratory for Research in Galaxies and Cosmology, Shanghai Astronomical Observatory, Chinese Academy of Sciences, 200030 Shanghai, People's Republic
of China

Abstract

Radio emission from the high- and super-Eddington accreting active galactic nuclei (AGNs) has various origins: a persistent jet, the magnetized corona, and the wind-like outflows. It is still unclear which is the leading mechanism responsible for the observed radio emission and how the radio emission is related to other characteristic parameters such as the Eddington ratio and black hole mass. In this paper, we present the 5 GHz Very Large Array (VLA) observational results of a sample of 25 extremely high Eddington accreting supermassive black holes (EESBHs, the Eddington ratio $\lambda_{\rm Edd}$ close to or above 1) in narrow-line Seyfert 1 galaxies, among which 22 sources are detected. Most of the EESBHs show a compact radio structure from a few hundred parsecs to 1 kpc scale. We estimated the lowest star formation rate surface density required for producing the observed radio emission and found that it is higher than the largest value previously detected in circumnuclear starburst galaxies, implying that the radio emission is from the AGN activity. Along with a comparison sample, we find an overall inverse $\mathcal{R}-\lambda_{\rm Edd}$ correlation ranging from sub- to super-Eddington ratios. The high-Eddington and mildly super-Eddington AGNs ($-0.5 < \log \lambda_{\rm Edd} < 0.6$) have a radio-to-X-ray luminosity ratio $L_{\rm R}/L_{\rm X} \sim 10^{-5}$–$10^{-4}$ and a steep radio spectrum, supporting that the radio emission is from transient ejecta (outflows) of corona; however, the jet contribution cannot be entirely ruled out. Our highly super-Eddington sources ($\log \lambda_{\rm Edd} \gtrsim 0.6$) have a flatter radio spectrum, along with its low radio luminosity: $L_{\rm R}/L_{\rm X} \sim 10^{-5}$; their radio emission is likely dominated by a magnetized corona, and a radiation-pressure-caused jet is also proposed in this paper.

Unified Astronomy Thesaurus concepts: Supermassive black holes (1663); Active galaxies (17); Jets (870); Active galactic nuclei (16)

1. Introduction

With increasing observational evidence during the past two decades, it is now widely accepted that supermassive black holes (SMBHs) with $M_{\rm BH} \sim 10^{5-10}\,M_\odot$ reside at the centers of most galaxies (see review in Kormendy & Ho 2013). The growth of SMBHs is believed to primarily occur through gas accretion, which gives rise to a luminous active galactic nucleus (AGN) with a large energy release in the form of radiation. The total energy radiated by this process cannot exceed the Eddington luminosity for the spherically symmetric accretion, which was thought to be the main mechanism for regulating the growth of SMBHs. However, observations have shown that super-Eddington accretion can occur in a variety of celestial systems, such as Galactic X-ray binaries (XRBs), e.g., SS 433 (Gies et al. 2002; Begelman et al. 2006; Fabrika et al. 2015; Middleton et al. 2018) and GRS 1915+105 (Mirabel & Rodríguez 1994; Greiner et al. 2001); tidal disruption events (TDEs, e.g., Bloom et al. 2011; Burrows et al. 2011; Levan et al. 2011; Zauderer et al. 2011; Auchettl et al. 2017; Dai et al.

2018; Wu et al. 2018); and narrow-line Seyfert 1 galaxies (NLS1s; e.g., Lanzuisi et al. 2016). Moreover, the violation of the Eddington limit becomes increasingly important for various related topics, including black hole growth, galaxy evolution, and AGN feedback, e.g., in ultraluminous X-ray sources (ULXs; see Kaaret et al. 2017, and references therein) with stellar-mass black hole/neutron stars and in primordial massive black holes during their early rapid growth (e.g., Volonteri & Rees 2005; Volonteri et al. 2015; Takeo et al. 2018).

The accretion states and their transitions in XRBs are now well studied using the hardness–intensity diagrams (HIDs), which are also coupled with radio emission (and hence the jets) and the Eddington ratios. It has been proposed frequently that AGNs experience accretion state transitions (e.g., Körding et al. 2006) in a similar way to XRBs in the framework of AGN-XRB unification (Falcke et al. 2004) but with substantially longer timescales ($>10^5$ yr; e.g., Schawinski et al. 2015). It is thus possible to connect these compact accreting systems by using scaling relations in parameter space with the most fruitful scheme of the triple correlation among X-ray luminosity, radio luminosity, and black hole mass (i.e., the so-called fundamental plane relation; Merloni et al. 2003). However, the fundamental plane relation is found to be

successful only in unifying low-luminosity AGNs and XRBs in the hard state.

The persistent jets are ubiquitous at low accretion rates (the low/hard state) in XRBs but intermittent or entirely absent at high accretion rates (the high/soft state and the intermittent/very high state; e.g., Meier 1996; Fender et al. 1999, 2004). Resembling the inverse correlation between the radio luminosity of jets and X-ray luminosity in XRBs, Ho (2002) found a similar inverse correlation between radio-loudness ($\mathcal{R} \equiv L_{\nu_5}/L_{\nu_B}$) and the Eddington ratio ($\lambda_{Edd} \equiv L_{bol}/L_{Edd}$) in AGNs. In this scheme, radio-loud AGNs with powerful relativistic jets often have low Eddington ratios, and vice versa. In contrast to the fundamental plane relation only being valid for certain conditions, the inverse correlation between $\mathcal{R}$ and λ_{Edd} is ubiquitous in both AGNs and XRBs (e.g., Broderick & Fender 2011) although with a large scatter. A global analogy between stellar-mass black holes and SMBHs has been established in the $\mathcal{R}$ and λ_{Edd} correlation: low-luminosity AGNs are similar to XRBs in the low/hard state, and with the high- or super-Eddington accreting AGNs (e.g., NLS1s) being an analogy of XRBs in the high/soft and the very high state. It should be noted here that only a few XRBs experience transitions from classical spectral states to the super-Eddington regime (e.g., Neilsen & Lee 2009). The super-Eddington accretion state is poorly understood primarily because of the extremely short timescales of the spectral state transition in XRBs. Therefore, the study of the production and quenching of AGN jets in super-Eddington accretion systems will shed light on the physical properties of AGNs during this short-lived spectral state.

The dynamic timescale in different accretion states is proportional to the mass of the central black hole. It is difficult to observe a complete burst cycle in individual AGNs resembling XRBs. Still, progress has been made by Sikora et al. (2007), providing further confirmation of the $\mathcal{R}$–λ_{Edd} inverse correlation with the Eddington ratio range from sub- to super-Eddington ratios in both radio-loud and radio-quiet AGNs. In this paper, the short-lived super-Eddington accreting AGNs will be studied to augment the correlation in the super-Eddington regime with robust measurements of the radio-loudness and the Eddington ratio.

Greene et al. (2006) have found that AGNs with super-Eddington accretion rates are predominately radio-quiet. The radio emission from radio-quiet AGNs can have various origins (see Panessa et al. 2019, and references therein), including persistent jets, a magnetized corona/jet base, and a wind-like outflow. In this paper, the "jets" especially refer to a collimated outflow. Furthermore, star-forming activities in the host galaxy may also contribute to the thermal and nonthermal radio emission, which typically shows host-like extension, with a diffused and clumpy structure, and has a low surface brightness. Nuclear starbursts have been observed in some galaxies (e.g., Deo et al. 2006; Hennig et al. 2018), and a significant fraction of the NLS1s tend to have circumnuclear star-forming rings (Deo et al. 2006), making them more difficult to distinguish from AGNs. These different mechanisms are fundamentally crucial in super-Eddington accreting AGNs and in explaining the $\mathcal{R}$–λ_{Edd} correlation.

As mentioned above, the origin of the radio emission from the super-Eddington accreting AGN itself is complicated. The slim-disk model was first proposed by Abramowicz et al. (1988) to describe a super-Eddington accretion flow. Recently,

progress has been made in simulating the super-Eddington accretion disk (e.g., Dotan & Shaviv 2011; Begelman & Volonteri 2017; Jiang et al. 2019), and several models among them support the launching of a jet, which is driven by either the radiation pressure (Takeuchi et al. 2009; Sádowski & Narayan 2015) or the magnetic field retrieved from the spin of the central black hole, i.e., a Blandford-Znajek (BZ) jet (Blandford & Znajek 1977) (e.g., Narayan et al. 2003; Kelley et al. 2014; McKinney et al. 2015). From observations, several super-Eddington accreting systems are found to accelerate a jet, and the trigger has been attributed to either a radiation pressure (e.g., Ohsuga & Mineshige 2011; Sádowski & Narayan 2015) or the BZ magnetic field (e.g., Berger et al. 2012). Furthermore, a super-Eddington accretion disk may also drive a strong wind and accelerate relativistic electrons to produce the observed synchrotron radio emission. For example, in SS 433, such wind-like radio-emitting outflows coexist with a relativistic jet, and they have a comparable radio luminosity (e.g., Blundell et al. 2001). In AGN accretion models, a hot $T_b \sim 10^9$ K corona in the vicinity of the black hole accretion disk may explain the observed X-ray emission from AGNs (Haardt & Maraschi 1991). It has been suggested that a magnetically heated corona may also produce the radio emission (Laor & Behar 2008; Raginski & Laor 2016). This hypothesis is later supported by the discovery of the similar radio-to-X-ray luminosity ratio $L_R/L_X \sim 10^{-5}$ between radio-quiet quasars and coronally active stars (Laor & Behar 2008) and by high radio frequency ($\gtrsim$100 GHz) observations of two nearby Seyfert galaxies (Behar et al. 2015, 2018; Inoue & Doi 2018).

Based on the topics mentioned above, the NLS1 galaxies may be introduced as a long-lived high Eddington ratio laboratory with an SMBH engine. NLS1s consist of a distinct class of AGNs identified by the width of their Hβ emission lines ($<$2000 km s^{-1}; Osterbrock & Pogge 1985; Boroson & Green 1992). They are located at an extreme end of the AGN parameter space that is believed to be governed mainly by the Eddington ratio (e.g., Boroson & Green 1992). Indeed, there is growing evidence showing that NLS1s have higher Eddington ratios and lower black hole masses than normal Seyfert 1 galaxies and quasars (e.g., Boroson & Green 1992; Du et al. 2015), which implies that they are systems with rapidly accreting SMBHs. NLS1s are often radio-quiet in contrast to the broad-line AGNs (e.g., Ulvestad et al. 1995). Interestingly, NLS1s are not completely radio quiescent, and the origin of their weak radio emission holds the long controversy. Several papers have presented evidence for the presence of radio jets in a handful of radio-quiet NLS1s (e.g., Lal et al. 2004; Giroletti & Panessa 2009; Doi et al. 2013, 2015), which is far from a consensus. However, as a subclass, the super-Eddington accreting NLS1s have not been comprehensively studied before. To study the super-Eddington accretion and investigate the origin of the radio emission in extremely high Eddington ratio accreting AGNs, we present high-resolution (subkiloparsec-scale) VLA results of a sample of NLS1s that are accreting at Eddington ratios close to or exceeding 1.

This paper is organized as follows: In Section 2 we describe our sample. Section 3 presents the procedure of data reduction. Sections 4 and 5 provide results from data reduction and analysis, followed with the discussion in Section 6. Throughout this paper we assume the same ΛCDM cosmology as in Sikora et al. (2007) and Broderick & Fender (2011), which is $H_0 = 100$ hr $= 70$ km s^{-1} Mpc^{-1}, $\Omega_M = 0.3$, and $\Omega_\Lambda = 0.7$.

Table 1
Information of Our EESBHs

Short Name	Alias	z	$M_{\rm BH}$ ($\times 10^7\,M_\odot$)	$\log f_{(2-10{\rm keV})}$ (erg cm^{-2} s^{-1})	$\log L_{\rm B}$ (erg s^{-1})	$\log L_{\rm bol}$ (erg s^{-1})	$\lambda_{\rm Edd}$
(1)	(2)	(3)	(4)	(5)	(6)	(7)	(8)
J0006+2012	Mrk 335	0.026	1.27	−10.73	43.55	44.90−45.71[a]	0.48−3.11
J0041+4021	Mrk 957	0.071	0.14	−12.30	43.27	>44.27	>1.02
J0053+1241	IZw1	0.059	2.38	−11.07	44.46	45.50−45.68[b]	1.02−1.54
J0107+1408	SDSS J010712.04+140845.0	0.076	0.09	−12.73	42.75	>43.75	>0.49
J0207+0242	Nab 0205+024	0.156	4.54	−11.30	44.72	>45.72	>0.90
J0230−0859	Mrk 1044	0.016	0.18	−11.16	42.91	45.08−46.04[a]	5.14−46.81
J0444+1221	IRAS 04416+1215	0.089	1.96	−11.80	44.07	46.60−47.55[a]	15.63−139.31
J1014−0418	PG 1011−040	0.058	2.12	−13.06	44.15	>45.15	>0.51
J1025+5140	Mrk 142	0.045	0.93	−11.13	43.40	45.74−46.60[a]	4.54−32.96
J1034+3938	KUG 1031+398	0.042	0.25	−12.06	43.24	45.01[c]	3.15
J1118+4025	PG 1115+407	0.155	2.60	−11.81	43.91	45.88[c]	2.24
J1140+0307	SDSS J114008.71+030711.4	0.081	0.09	−12.59	42.94	45.07[c]	10.04
J1153+4612	Mrk 42	0.025	0.09	−11.61	42.48	>43.48	>0.26
J1242+3317	IRASF 12397+3333	0.043	0.59	−11.24	43.05	46.04−46.92[a]	14.32−108.64
J1246+0222	PG 1244+026	0.048	0.19	−11.64	43.39	45.48[c]	12.24
J1355+5612	RX J1355.2+5612	0.122	0.93	−12.08	43.94	>44.94	>0.72
J1405+2555	PG 1402+261	0.164	3.93	−11.64	44.08	46.02[c]	2.05
J1431+2817	Mrk 684	0.046	0.69	−11.58	43.67	>44.67	>0.53
J1442+3526	Mrk 478	0.077	2.32	−11.57	44.40	45.64[d]	1.44
J1451+2709	PG 1448+273	0.065	1.03	−11.69	44.09	45.83[c]	5.05
J1536+5433	Mrk 486	0.039	0.90	−11.36	43.32	44.42−45.23[a]	0.22−1.45
J1559+3501	Mrk 493	0.031	0.10	−11.42	42.92	44.86[c]	5.58
J1703+4540	B3 1702+457	0.060	0.38	−11.23	43.47	>44.47	>0.60
J2236+1343	PG 2233+134	0.326	8.21	−12.29	44.81	47.13[d]	12.64
J2242+2943	Akn 564	0.025	0.21	−10.62	43.25	44.50[e]	1.15

Notes. Column (1): short name. Column (2): alias. Column (3): redshift. Column (4): black hole mass estimated from broad emission line (see Wang et al. 2013). Column (5): 2–10 keV X-ray flux density. Column (6): k-corrected B-band optical luminosity of AGNs (erg s^{-1}), calculated from 5100 Å flux density f_{5100}, fraction of AGN contribution at 5100 Å, and an assumed optical spectral index $\alpha_{\rm opt} = -0.5$. Column (7): bolometric luminosity (erg s^{-1}) and references. Column (8): Eddington ratio.

References.
[a] Castelló-Mor et al. (2016)
[b] Martínez-Paredes et al. (2017)
[c] Jin et al. (2012b)
[d] Runnoe et al. (2012)
[e] Ricci et al. (2013)

2. The Sample

Our parent sample is composed of 60 super-Eddington accreting SMBH candidates with Eddington ratios close to or above 1, which was compiled by Wang et al. (2013). Given a strong relation between the Eddington ratio $\lambda_{\rm Edd}$ and the X-ray photon index $\Gamma_{2-10\,\rm keV}$ (e.g., Lu & Yu 1999; Brightman et al. 2013), AGNs with higher Eddington ratios are expected to have a steeper hard X-ray photon index $\Gamma_{2-10\,\rm keV}$ according to this well-known relation. The super-Eddington AGN candidates have actually been selected indirectly by having $\Gamma_{2-10\,\rm keV} > 2$. This selection approach requires an accurate determination of their bolometric luminosities $L_{\rm bol}$ and the knowledge of the broadband spectral energy distribution (SED; e.g., Jin et al. 2017). Unfortunately, it is difficult to measure $L_{\rm bol}$ from broadband SED since much of the radiation from the accretion disk is in the form of extreme-ultraviolet, which is beyond the observation windows. Still, accurate bolometric luminosity measurements (by using SED fitting) have been obtained from the literature for most of our super-Eddington AGN candidates (see Column (7) of Table 1 and the corresponding references) with a robust mass determination.

To study the radio emission from super-Eddington AGNs, we have searched our parent sample for available high-resolution radio observations in the Very Large Array (VLA) data archive. We primarily collected VLA observations at C and X band with the A-array configuration having a resolution corresponding to a projected linear size $\lesssim 2$ kpc at the rest frame of each object. Furthermore, we also collected L-band observations with the VLA A-array when there were no high-resolution observational data at C and X bands. Twenty-six sources meet the requirements, which also includes an intrinsic radio-loud NLS1, 1H 0323+342 (Zhou et al. 2007), that has been detected in γ-rays by Fermi-LAT (Abdo et al. 2009). Observations show that the radio emission in this source is strongly Doppler boosted (e.g., Hada et al. 2018). This source was removed from our final sample of 25 objects. The basic information of the objects used for this research is listed in Table 1. The black hole mass and 2–10 keV flux density are obtained from Wang et al. (2013), where the black hole mass was estimated by using the broad emission line width and the 5100 Å luminosity. However, the relationship between the broad-line region size and 5100 Å luminosity for super-Eddington accretion SMBHs might be different from the normal relation, which may induce further uncertainty in the

black hole mass estimation (see Czerny et al. 2019, and references therein). Among 25 objects in our final sample, 16 (∼64%) objects are at the super-Eddington regime, whereas the remaining 9 (36%) are high-Eddington sources. For this reason, the super-Eddington accreting AGN candidates used in this work will be referred to as extremely high Eddington ratio accreting supermassive black holes (EESBHs) with an Eddington ratio close to or above 1.

3. VLA Data Reduction

All the relevant raw data (visibilities) have been retrieved from the NRAO Data Archive,[9] and only the data with good quality and the correct observational configurations have been adopted. In general, each target should have been observed for more than 20 s for historical VLA data, but there is no such restriction for the Karl G. Jansky VLA (JVLA) data. Each data set should contain one exposure of a nearby phase calibrator. Although some results have already been published (see Table 2), in order to ensure uniformity of analysis across all the parameters, we performed a manual calibration for all the data sets using the Common Astronomy Software Application (CASA v5.1.1; McMullin et al. 2007). The archive data have a time range from 1980 to 2016 and are composed of two distinct groups, the historical or ordinary VLA products and the JVLA products. The historical VLA data sets were scheduled as a single channel in only one or two spectral windows (SPWs), while the JVLA continuum observations are all in the multi-SPW mode, with each SPW having a good bandwidth coverage.

Our data analysis followed the standard routines described in the CASA Cookbook. Each observation includes at least one primary calibrator for the calibration of the flux density scale; in total, there are four primary calibrators used in our data sets, i.e., 3C 286, 3C 48, 3C 138, and 3C 147. We adopted the closest flux density standard concerning the observing date to get the absolute flux density for the primary flux calibrator. Subsequently, we bootstrapped onto the secondary flux density calibrators and targets. For example, we use the flux density standards "Perley-Butler 2013" (Perley & Butler 2013) to set the overall flux density scale for data sets from the project 15A-283 running from 2015 July to September. For the historical VLA data sets, we determined the gain solutions by using a nearby secondary calibrator and transferred them to target sources. In contrast to using a narrow band in historical VLA data sets, the JVLA data sets were all scheduled with multiple channels and spectral windows. We thus referred to the calibrating scheme/routine as described in the most recent CASA Cookbook. In addition to transferring the flux density scale and gain solutions, antenna delay and bandpass corrections were also determined by fringe-fitting the visibilities.

Deconvolution, self-calibration, and model fitting were performed in the DIFMAP software package (Shepherd et al. 1994). The final images are created with natural weighting. Only for sources with a high signal-to-noise ratio (S/N > 9) was self-calibration applied using a well-established model. The self-calibration was performed initially only on phase, and subsequently on both phase and amplitude when we achieved a good model. A two-dimensional Gaussian model was used to fit each target's visibility data to obtain characteristic parameters, such as the integrated and peak flux density, as

---
9 https://archive.nrao.edu/archive/advquery.jsp

well as the FWHM of the Gaussian model. The model fitting results are listed in Table 3. Furthermore, we have presented the flux densities for two sources (J1140+0307 and J1431 +2817) with marginal detections, i.e., only a $\gtrsim 3\sigma$ component appearing in the image center, which is marked with "∼" in Columns (4) and (5) of Table 3. For the sources without a significant detection, we adopt 3σ flux density upper limit.

We estimated the uncertainty of the integrated flux density S_i based on the formulae given by Hopkins et al. (2003). As most of our targets have an unresolved point-like nucleus (42 out of 45 data sets have a peak-to-total flux density ratio >0.80), the relative errors of the integrated flux density S_i were estimated from $\sigma_i / S_i = \sqrt{2.5\sigma_{rms}^2 / S_p^2 + 0.01^2}$ (Hopkins et al. 2003, Equation (5)). The uncertainty of the peak flux density was estimated by combining the model fitting errors and the initial calibrating errors, which is $\sigma_p = \sqrt{\sigma_{rms}^2 + (1.5\sigma_{rms})^2} \approx 1.8\sigma_{rms}$ (Hovatta et al. 2012, see their Appendix B), where $1.5\sigma_{rms}$ comes from the CLEAN error and σ_{rms} is the experimental error, where σ_{rms} is the rms noise estimated in a blank-sky zone far away from each target source.

In addition, we have performed some additional data reduction procedures for a few sources:

1. *J0444+1221 (IRAS 04416+1215)*: there are no available VLA data at C band for this source. Alternatively, we estimated a C-band flux density by using the L-band to X-band spectral index ($\alpha_{1.4}^{8.4} = -0.91$); the resulting 5 GHz flux density is 4.07 mJy.
2. *J1242+3317 (IRAS 12397+3333)*: this source shows diffused emission with a linear extension along the major axis of its host galaxy. This radio structure can be modeled with four Gaussian components. Here we only take into account the flux density from the central compact component as the integrated flux of the core.
3. *J1431+2817 (Mrk 684)*: The VLA A-array observation at C band has a baseline range from 0 to 0.6 Mλ. Here we constrain the baseline to be >0.04 Mλ; this procedure rejects some diffused emission and results in a detection of the central source with a peak flux density of ∼0.05 mJy beam^{-1}, but the S/N is only 3.3.
4. *J2242+2943 (Akn 564)*: We have measured a peak flux density of 5.69 ± 0.03 mJy beam^{-1} at C band, which is consistent with the peak flux density of 5.68 ± 0.02 mJy beam^{-1} obtained by Berton et al. (2018). The source is resolved into three components at C and X bands. We only consider the integrated flux density of the central component, which is 5.84 ± 0.03 mJy at C band and 3.18 ± 0.07 mJy at X band. Schmitt et al. (2001) also fit the X-band image with three components, and the inferred integrated flux density of the central component is 3.1 mJy, which is consistent with our results. The size of the radio structure is ∼2″ (corresponding to a physical linear size of ∼4 kpc).

4. Results

The new results for 25 EESBHs observed with the VLA are obtained from a total of 45 data sets, of which 26 were previously published (see the references in Column (10) of Table 2), and the remaining 19 data sets are analyzed in this work. All but one object (J0444+1221) has C-band data, and 22 out of 24 objects are detected at C band with a peak flux

Table 2
Summary of VLA A-array Observations

Short Name	Receiver	Obs. ID	Date	Time (s)	Bandwidth (MHz)	θ_{maj} (arcsec)	θ_{min} (arcsec)	P.A. (deg)	References
(1)	(2)	(3)	(4)	(5)	(6)	(7)	(8)	(9)	(10)
J0006+2012	C band	15A-283	2015-07-05	538	2048	0.44	0.38	55.3	b
	L band	AM0384	1992-12-31	920	100	1.68	1.49	−35.5	
	X band	AM0384	1992-12-31	1050	100	0.25	0.23	−40.0	
J0041+4021	C band	AH0221	1986-05-18	2070	100	0.48	0.38	−10.9	
	L band	AL0502	1999-08-26	330	100	1.44	1.40	66.0	
J0053+1241	C band	AC0624	2002-05-02	590	100	0.45	0.39	2.7	
	L band	AK0406	1995-07-20	370	100	1.55	1.32	−3.2	
	X band	AB0670	1992-12-04	7160	100	0.26	0.24	24.4	
J0107+1408	C band	AG0670	2004-10-10	1713	100	0.43	0.38	8.3	g
J0207+0242	C band	AH0333	1989-01-09	840	100	0.63	0.40	41.0	
	L band	WARD	1982-03-04	690	100	1.75	1.38	32.5	
J0230−0859	C band	AU0028	1987-07-29	1310	100	0.70	0.39	−32.0	a
	L band	AU0028	1987-07-29	690	100	2.30	1.27	−32.0	a
	X band	AS0727	2002-02-16	1170	100	0.45	0.23	−38.2	
J0444+1221	L band	AM0492	1995-07-10	340	100	1.50	1.28	2.5	
	C band	AM0492	1995-07-10	330	100	0.25	0.21	7.3	
J1014−0418	C band	AK0096	1983-11-21	1470	100	0.66	0.38	−37.3	c
J1025+5140	C band	AK0096	1983-11-20	1350	100	0.46	0.41	50.7	c
J1034+3938	C band	15A-283	2015-08-29	598	2048	0.47	0.40	83.8	b
J1118+4025	C band	AK0096	1983-11-20	1430	100	0.43	0.41	71.6	c
J1140+0307	C band	AG0670	2004-10-10	2819	100	0.53	0.39	−34.2	g
J1153+4612	C band	AU0028	1987-07-31	1790	100	0.50	0.40	58.8	a
J1242+3317	C band	15A-283	2015-09-06	553	2048	0.45	0.36	83.0	b
J1246+0222	C band	15A-283	2015-09-06	553	2048	0.52	0.41	−42.3	b
J1355+5612	C band	15A-283	2015-08-30	553	2048	1.14	0.38	60.5	b
J1405+2555	C band	AK0096	1983-11-14	1470	100	0.42	0.39	−15.9	c
	L band	AD0302	1992-12-11	730	100	1.46	1.34	−22.1	
J1431+2817	C band	AU0028	1987-07-31	1800	100	0.49	0.42	−37.8	a
J1442+3526	C band	AK0096	1983-11-20	1420	100	0.43	0.42	−69.5	c
	L band	AG0574	1999-09-25	315	100	1.24	1.16	−59.5	e
	X band	AG0574	1999-09-25	430	100	0.24	0.23	46.2	e
J1451+2709	C band	AK0096	1983-11-20	1430	100	0.45	0.41	−36.4	c
J1536+5433	C band	15A-283	2015-08-29	658	2048	0.66	0.37	82.9	b
J1559+3501	C band	15A-283	2015-07-23	523	2048	1.30	0.34	59.9	b
	L band	AG0777	2008-12-05	1163	100	1.43	1.42	67.6	
	X band	12B-064	2012-10-25	3590	2048	0.24	0.19	−63.1	f
J1703+4540	C band	15A-283	2015-07-22	538	2048	0.73	0.39	77.9	b
	L band	AM0492	1995-07-12	330	100	1.60	1.38	−70.6	
	X band	AM0492	1995-07-12	320	100	0.27	0.23	−71.7	
J2236+1343	C band	AK0096	1983-11-23	1530	100	0.51	0.40	−44.2	c
	L band	AH0291	1987-10-11	300	50	1.49	1.28	−15.2	
	X band	AG0499	1996-10-29	3720	100	0.27	0.25	4.6	
J2242+2943	C band	15A-283	2015-07-02	598	2048	0.50	0.43	65.4	b
	L band	AL0502	1999-08-26	320	100	1.49	1.38	−25.5	
	X band	AB0973	2000-11-14	1310	100	0.23	0.21	−4.0	d

Note. Column (1): short name. Column (2): observational bands. Column (3): project ID. Column (4): observing date. Column (5): observing time of target source. Column (6): observing bandwidth. Columns (7)–(9): beam major axis, minor axis, and position angle. Column (10): references for data set publication.
References. (a) Ulvestad et al. 1995; (b) Berton et al. 2018; (c) Kellerman et al. 1989; (d) Schmitt et al. 2001; (e) Kinney et al. 2000; (f) Gültekin et al. 2014; (g) Greene et al. 2006.

density above 3σ. All the sources were observed with a resolution of <2 kpc at C band, while 20 out of 24 sources were observed with a resolution of <1 kpc. Table 3 lists the 5 GHz luminosity (Column (8)), the radio brightness temperature (Column (9)), and radio-loudness (Column (10)).

The radio brightness temperature was estimated by using the formula (e.g., Ulvestad et al. 2005)

$$T_{\mathrm{B}} = 1.8 \times 10^9 (1 + z) \frac{S_i}{\nu^2 \theta^2} \; (\mathrm{K}), \qquad (1)$$

where S_i is the integrated flux density of each Gaussian model component in units of mJy (Column (5) of Table 3), θ is the FWHM of the Gaussian model in milliarcseconds (Column (7) of Table 3), ν is the observing frequency in GHz (Column (2) of Table 3), and z is the redshift. The estimated 5 and 8.4 GHz radio brightness temperatures are listed in Column (9) of Table 3. Because the measured component size is just the upper limit, the radio brightness temperature should be considered as a lower limit. The nonsimultaneous 5–8 GHz spectral indices α

Table 3
Observational Results and Model Fitting Parameters

Short Name (1)	Freq. (GHz) (2)	Res. (kpc) (3)	S_p (mJy beam^{-1}) (4)	S_i (mJy) (5)	rms (μJy) (6)	θ (mas) (7)	log L_5 (erg s^{-1}) (8)	log T_B (K) (9)	$\mathcal{R}$ (10)	$\alpha_5^{8.4}$ (11)	log Σ_{SFR} ($M_\odot$ yr^{-1} kpc^{-2}) (12)
J0006+2012	5.17	0.20	3.04 ± 0.03	3.21 ± 0.02	17.06	92.61	38.44	4.40	1.05	−0.84	2.13
	1.42	0.80	6.15 ± 0.33	6.19 ± 0.29	184.79	277.85					0.79
	8.43	0.12	1.92 ± 0.07	2.14 ± 0.06	39.25	60.59		4.18			2.58
J0041+4021	4.86	0.53	1.61 ± 0.08	2.08 ± 0.09	44.74	246.43	39.11	3.44	9.56		1.95
	1.42	1.95	5.82 ± 0.21	6.78 ± 0.22	119.44	∼400.00					0.99
J0053+1241	4.86	0.45	1.85 ± 0.11	1.89 ± 0.10	64.90	61.95	38.90	4.59	0.37	−1.11	1.91
	1.42	1.55	4.63 ± 0.29	4.91 ± 0.27	161.83	291.11					0.83
	8.43	0.28	0.82 ± 0.02	1.02 ± 0.03	15.70	122.42		3.26			2.28
J0107+1408	4.86	0.56	<0.06	<0.06	22.28		<37.67		<1.13		0.51
J0207+0242	4.86	1.11	1.17 ± 0.10	1.23 ± 0.10	60.94	133.26	39.61	3.78	1.04		1.71
	1.46	3.84	2.85 ± 0.29	2.95 ± 0.27	166.59	311.50					0.69
J0230−0859	4.86	0.13	0.44 ± 0.11	0.44 ± 0.09	61.74	55.12	37.12	4.05	0.22	−0.73	1.02
	1.48	0.42	1.09 ± 0.37	1.10 ± 0.32	207.25						−0.02
	8.46	0.07	0.28 ± 0.07	0.29 ± 0.07	43.90	68.89		3.20			1.46
J0444+1221	5.00			∼4.07			∼39.62		∼4.88		
	1.42	2.19	12.14 ± 0.28	12.83 ± 0.26	158.73	317.15					1.32
	8.43	0.36	2.04 ± 0.12	2.52 ± 0.13	70.82	113.48		3.73			2.79
J1014−0418	4.86	0.44	0.47 ± 0.13	0.48 ± 0.11	73.44	62.94	38.30	3.99	0.19		1.16
J1025+5140	4.86	0.37	0.19 ± 0.07	0.22 ± 0.07	40.03	117.40	37.73	3.10	0.29		0.92
J1034+3938	5.17	0.34	6.75 ± 0.01	6.98 ± 0.01	10.06	78.36	39.19	4.90	12.18		2.44
J1118+4025	4.86	1.13	<0.16	<0.16	54.23		<38.72		<0.86		0.97
J1140+0307	4.86	0.61	∼0.05 ± 0.02	∼0.06 ± 0.03	16.13	∼214.29	∼37.68	∼2.02	∼0.76		0.36
J1153+4612	4.86	0.20	0.21 ± 0.09	0.22 ± 0.08	54.19	209.30	37.22	2.61	0.75		0.88
J1242+3317	5.17	0.31	1.53 ± 0.02	1.37 ± 0.02	14.58	127.77	38.51	3.77	3.87		1.80
J1246+0222	5.17	0.39	0.92 ± 0.04	0.85 ± 0.03	22.28	80.06	38.40	3.97	1.38		1.48
J1355+5612	5.17	0.86	2.11 ± 0.05	2.23 ± 0.04	29.09	128.06	39.67	4.00	7.30		1.70
J1431+2817	4.86	0.39	∼0.05 ± 0.02	∼0.05 ± 0.02	15.78	∼156.97	∼37.09	∼2.20	∼0.03		0.23
J1442+3526	4.86	0.63	0.96 ± 0.10	1.83 ± 0.17	59.15	510.15	39.13	2.76	0.73	−2.09	1.91
	1.42	1.74	3.65 ± 0.31	5.55 ± 0.42	176.10	842.75					1.06
	8.46	0.34	0.31 ± 0.11	0.57 ± 0.18	63.17	219.44		2.50			2.11
J1405+2555	4.86	1.13	0.26 ± 0.05	0.27 ± 0.04	31.20	93.90	39.00	3.43	1.13		1.25
	1.42	3.89	0.93 ± 0.29	0.95 ± 0.26	163.47	77.54					0.29
J1451+2709	4.86	0.52	1.37 ± 0.09	1.43 ± 0.09	55.42	86.13	38.87	4.19	0.81		1.77
J1536+5433	5.17	0.29	0.64 ± 0.02	0.65 ± 0.02	15.36	18.93	38.10	5.10	0.81		1.29
J1559+3501	5.17	0.21	0.48 ± 0.02	0.62 ± 0.03	15.64	286.15	37.87	2.72	1.20	−0.17	1.00
	1.40	0.90	2.11 ± 0.33	2.85 ± 0.39	183.58	1089.62					0.54
	8.84	0.16	0.56 ± 0.01	0.56 ± 0.01	4.56	18.21		4.60			2.13
J1703+4540	5.10	0.46	26.39 ± 0.03	27.50 ± 0.03	19.01	92.85	40.10	5.36	58.00	−0.56	2.88
	1.42	1.65	99.26 ± 0.36	107.89 ± 0.34	200.73	276.37					2.14
	8.43	0.27	20.21 ± 0.15	20.73 ± 0.13	85.34	49.39		5.35			3.59
J2236+1343	4.86	1.94	0.24 ± 0.09	0.24 ± 0.07	50.71	394.22	39.61	2.19	0.86	1.07	1.32
	1.47	6.22	0.92 ± 0.30	0.90 ± 0.26	171.49	169.46					0.51
	8.46	1.21	0.42 ± 0.03	0.43 ± 0.02	18.19	62.41		3.57			2.25
J2242+2943	5.17	0.22	5.69 ± 0.03	5.84 ± 0.03	21.11	161.50	38.63	4.18	4.02	−1.23	2.33
	1.42	0.71	22.36 ± 0.85	24.92 ± 0.84	477.40	499.21					1.48
	8.46	0.10	2.81 ± 0.07	3.18 ± 0.07	40.87	94.40		3.96			2.83

Note. Column (1): short name. Column (2): central frequency. Column (3): physical resolution in kpc. Column (4): peak flux density; "∼" means that this source is only marginally detected, and for the sources that have not been detected we take the 3σ upper limit. Column (5): integrated flux; the C-band flux density for source J0444+1221 is estimated from L- and X-band data (marked with "∼"). Column (6): image noise rms. Column (7): FWHM of the Gaussian model. Column (8): 5 GHz radio luminosity. Column (9): lower limit of radio brightness temperature. Column (10): radio-loudness. Column (11): nonsimultaneous 5–8.4 GHz spectral index. Column (12): lower limit of SFR surface density estimated from radio luminosity.

(defined as $S_i \propto \nu^\alpha$) based on the integrated flux densities are listed in Column (11) of Table 3.

Next, we compared the radio emission at different galactic scales. For instance, the VLA A-array flux density at L band may be taken as a measurement of the core radio emission. The flux density derived from the Faint Images of the Radio Sky at Twenty-Centimeters (FIRST) 1.4 GHz survey (Becker et al. 1995) made with the VLA B-array may serve as a proxy of the radio emission from the entire galaxy. These two observations provide a projected spatial resolution of ∼4–8 kpc and ∼20–30 kpc, respectively. The typical size of the optical hosts of EESBHs in our sample is comparable to the VLA B-array beam size at 1.4 GHz (the FIRST images). For those sources without the FIRST survey coverage or without detection, the NRAO VLA Sky Survey (NVSS; Condon et al. 1998) flux density has been taken instead, and the 1.4 GHz flux densities are listed in Table 4; there are 11 sources in total. Figure 1

Short Name	J0006+2012	J0041+4021	J0053+1241	J0207+0242	J0230−0859	J0444+1221
Alias	Mrk 335	Mrk 957	IZw1	Nab 0205+024	Mrk 1044	IRAS 04416+1215
VLA-B/D	7.3 ± 0.5^N	16.4 ± 0.6^N	5.3 ± 0.1^F	2.7 ± 0.1^F	1.3 ± 0.1^F	13.9 ± 0.6^N
VLA-A	6.1 ± 0.1	6.7 ± 0.1	4.9 ± 0.1	2.9 ± 0.1	1.1 ± 0.2	12.8 ± 0.1
Short Name	J1405+2555	J1442+3526	J1559+3501	J1703+4540	J2242+2943	
Alias	PG 1402+261	Mrk 478	Mrk 493	B3 1702+457	Akn 564	
VLA-B/D	0.7 ± 0.1^F	3.3 ± 0.1^F	3.3 ± 0.1^F	118.6 ± 0.1^F	28.6 ± 0.9^N	
VLA-A	0.9 ± 0.1	5.5 ± 0.1	2.8 ± 0.1	107.8 ± 0.2	24.9 ± 0.4	

Note. 1.4 GHz flux density in mJy. ^{N}: NVSS; ^{F}: FIRST .
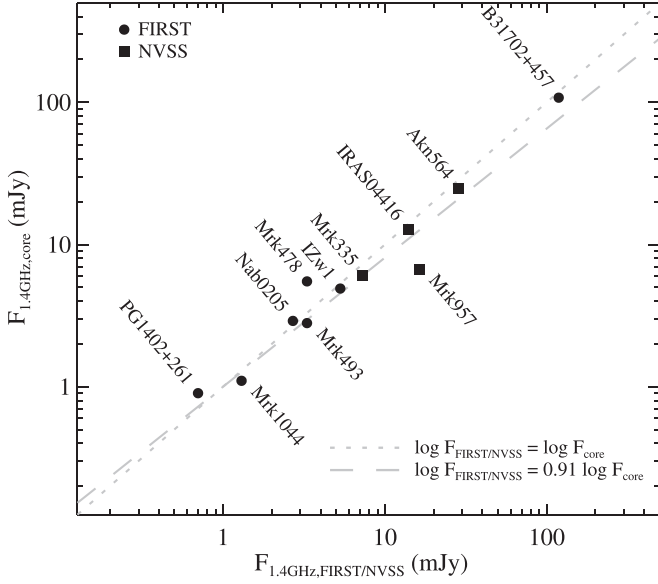
Figure 1. Comparison between the 1.4 GHz radio emission observed in VLA A-array and VLA B/D-array. The dotted and dashed lines indicate $\log F_{\text{FIRST/NVSS}} = \log F_{\text{core}}$ and $\log F_{\text{FIRST/NVSS}} = 0.91 \log F_{\text{core}}$, respectively.

shows the comparison between the FIRST/NVSS flux density and the VLA A-array 1.4 GHz flux density. Taking a 1σ uncertainty, the two fluxes are in good agreement for most sources. Nine out of 11 sources have a central flux density that accounts for >80% of the total radio emission. Among these sources, the average flux density difference between VLA A-array and FIRST/NVSS measurements is only 18% (Mrk 957 has a 59% VLA A-array flux density decrease by comparing it with the NVSS measurement). We have also marked a line $\log F_{\text{FIRST/NVSS}} = 0.91 \log F_{\text{core}}$ in Figure 1 to show the comparison between the FIRST/NVSS and the VLA A-array 1.4 GHz flux density. This indicates that most sources are compact at this resolution, and the radio emission is dominated by the central $\sim$4–8 kpc region. Furthermore, given the time lag between FIRST, NVSS, and the VLA A-array 1.4 GHz observations, we can infer that our EESBHs have a fairly stable radio emission.

5. Parameter Correlations

The correlation between the radio-loudness $\mathcal{R}$ and the Eddington ratio λ_{Edd} in the extremely high Eddington regime ($\lambda_{\text{Edd}} \gtrsim 1$) has not been well explored previously because of the limited number of super-Eddington sources and a poor

estimation of their Eddington ratios. In order to form a broad parameter space for the Eddington ratio, we include 199 AGNs from Sikora et al. (2007) having a wide range of Eddington ratios from $\log \lambda_{\text{Edd}} = -7$ to 1.

An accurate estimate of the bolometric luminosity is required to get the Eddington ratio λ_{Edd}, which is defined as $\lambda_{\text{Edd}} \equiv L_{\text{bol}}/L_{\text{Edd}}$. The integral of the observed SED of the optical−ultraviolet and X-ray emission by the accretion disk and the hot corona provides a direct measurement of the bolometric luminosity L_{bol}. One generally uses the B-band continuum luminosity L_B to estimate the bolometric luminosity with a bolometric correction factor κ_B expressed as $L_{\text{bol}} = \kappa_B L_B$. The commonly used B-band bolometric correction factor is $\kappa_B = 10$ (e.g., Marconi et al. 2004; McLure & Dunlop 2004). However, it is only suitable for sub-Eddington systems, as the high Eddington ratio sources tend to have a larger bolometric correction factor (see Vasudevan & Fabian 2007).

It was also noted by Jin et al. (2012a, 2012b) that NLS1s often possess high Eddington ratios, having significantly higher values of the optical bolometric correction factor than other samples. Surprisingly, the average value of 5100 Å bolometric correction factor $\kappa_{5100} \approx 70$ has been found for 10 NLS1s. Wang et al. (2013) independently got $\kappa_{5100} \approx 40 - 100$ for their super-Eddington accreting AGN candidates. The majority of high-Eddington sources in Sikora et al. (2007) are Palomar −Green (PG) quasars; therefore, instead of using a common bolometric correction factor, we use the bona fide bolometric luminosity that was obtained from the SED fitting to recalculate the Eddington ratios for PG quasars and our EESBHs. The bolometric luminosities for our EESBHs and PG quasars are presented in Table 1 (Column (7)) and Table 5, respectively. On the other hand, the B-band bolometric correction factor $\kappa_B = 10$ was used to set a lower limit of the Eddington ratios for those EESBHs without previous bolometric luminosity estimates.

The radio-loudness of these 199 sources is taken from Broderick & Fender (2011), measured based on the core-only radio emission. The strategy of using the core-only radio emission depends on the idea that the optical/X-ray radiation is only related to the current/recent nuclear activity, which is not directly correlated with large-scale radio emission. It was found that the jet emission can exist for a timescale of $\sim 10^7$–10^8 yr (e.g., Kuźmicz et al. 2018). On the other hand, the large-scale jet emission depends not only on the central engine itself but also on the surrounding environment, for example, as radio galaxies as well as radio-loud quasars reside in denser

Table 5
Bolometric Luminosities of PG Quasars

Name (1)	$\log L_{\mathrm{bol}}$ (erg s^{-1}) (2)	Name (3)	$\log L_{\mathrm{bol}}$ (erg s^{-1}) (4)	Name (5)	$\log L_{\mathrm{bol}}$ (erg s^{-1}) (6)	Name (7)	$\log L_{\mathrm{bol}}$ (erg s^{-1}) (8)
PG 0007+106	45.38[b]	PG 1103−006	46.30[a]	PG 1307+085	45.88[c]	PG 1534+580	44.43[a]
PG 0026+1298	46.16[c]	PG 1114+445	45.39[a]	PG 1309+355	45.74[a]	PG 1545+210	45.93[a]
PG 0052+251	45.94[a]	PG 1116+215	46.31[a]	PG 1351+640	45.30[a]	PG 1617+175	44.56−45.55[d]
PG 0804+761	45.47[b]	PG 1202+28	45.41[a]	PG 1352+183	45.61[a]	PG 2130+099	44.77[b]
PG 0844+349	45.31[a]	PG 1211+143	45.77[b]	PG 1411+442	45.33[a]	PG 2251+113	46.35[a]
PG 0923+129	45.32[b]	PG 1216+069	46.31[a]	PG 1415+451	45.37[a]		
PG 0953+414	46.42[a]	PG 1229+204	45.65[b]	PG 1426+015	45.65[b]		
PG 1100+772	46.46[a]	PG 1259+593	46.83[a]	PG 1444+407	46.19[a]		

Notes.
References.
[a] Runnoe et al. (2012).
[b] Martínez-Paredes et al. (2017).
[c] Vasudevan & Fabian (2007).
[d] Castelló-Mor et al. (2016).
[e] Jin et al. (2012b).

environments than radio-quiet AGNs (e.g., Lietzen et al. 2011). Besides, the star formation in host galaxies will also contribute significant radio emission on the whole galaxy scale. Since the radio-loudness and the Eddington ratio are relatively dependent on the optical or X-ray estimates, it is reasonable to adopt the core-only radio emission for the relation between radio-loudness and the Eddington ratio.

The standard radio-loudness parameter (Kellerman et al. 1989) is defined as $\mathcal{R} \equiv L_{\nu_5}/L_{\nu_B} = 1.3 \times 10^5 (L_5/L_B)$, where L_5 is the radio luminosity at 5 GHz and L_B is the optical luminosity of the nucleus at $\lambda_B = 4400$ Å; both are measured in erg s^{-1}. For our EESBHs, we have measured the core radio emission from the brightest component of the object. Nearly all of our EESBHs are unresolved with VLA A-array observation at 5 GHz (except for J2242+2943 or Akn 564), and most have a component size of a few hundred parsecs (except for four sources with relatively large redshift, i.e., $z > 0.15$). Therefore, the 5 GHz core-only radio emission of our EESBHs is consistent with Broderick & Fender (2011). Here the total radio luminosity is expressed as $L_5 \equiv \nu_5 L_{\nu_5}$ and the total B-band luminosity as $L_B \equiv \nu_B L_{\nu_B}$. In this paper, we calculate the B-band luminosity by using the 5100 Å luminosity using the transformation $L_B = L_{5100} \times (\lambda_B/5100)^{1+\alpha_{\mathrm{opt}}}$ and assuming a constant optical spectral index $\alpha_{\mathrm{opt}} = -0.5$ (e.g., Sikora et al. 2007). The radio luminosity is given as

$$L_{\mathrm{R}} = \nu_R f_R \frac{4\pi D_L^2}{(1+z)^{1+\alpha_R}}, \qquad (2)$$

where α_R is the radio spectral index, assuming $\alpha_R = -0.8$ according to our measurement of 5–8.4 GHz spectral index; f_R is the radio flux density; and D_L is the luminosity distance. Figure 2 shows the radio-loudness versus the Eddington ratio for 199 comparison AGNs and our EESBHs. Here we keep the traditional labels of the source sample for 199 comparison AGNs, and similarly hereinafter. By using all the data sets collected in Figure 2, we derived a linear regression slope between $\log \mathcal{R}$ and $\log \lambda_{\mathrm{Edd}}$ of -0.73 ± 0.08 within the 95% confidence interval; the blue belt shows the upper and lower boundaries corresponding to the slope of -0.73. Interestingly, we can see that there are a lot of vacancies at both the upper left
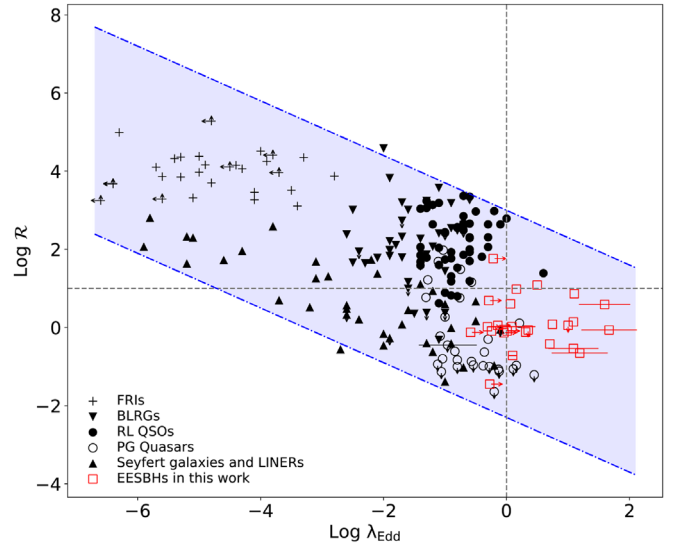

Figure 2. Radio-loudness $\mathcal{R}$ vs. Eddington ratio λ_{Edd}. The markers are designated in the lower left corner, and the error bars in some EESBH objects come from the uncertainty of the black hole spin. The vertical dotted line is $\lambda_{\mathrm{Edd}} = 1$, and the horizontal dotted line at $\mathcal{R} = 10$ represents the division between radio-loud (above) and radio-quiet (below) sources. The blue belt shows the upper and lower boundaries corresponding to a slope of -0.73.

and lower right corners in Figure 2, which implies that the sample in Figure 2 is incomplete for larger radio-loudness at the lower boundary of the Eddington ratios and also for both larger and lower radio-loudness at the higher boundary of Eddington ratios. However, the trend may also hint at real features of radio-loudness at higher and lower Eddington ratios.

The other problem is that the regression slope between $\log \mathcal{R}$ and $\log \lambda_{\mathrm{Edd}}$ is close to -1 and possibly governed by the mutual dependence of $\mathcal{R}$ and λ_{Edd} on optical luminosity, i.e., according to the definitions, $\mathcal{R} \propto L_B^{-1}$ and $\lambda_{\mathrm{Edd}} \propto L_{\mathrm{bol}}$, if we take the relation $L_{\mathrm{bol}} = 10 L_B$, then $\log \mathcal{R}$ versus $\log \lambda_{\mathrm{Edd}}$ is naturally akin to -1. That is indeed what we do for the samples in Figure 2 except for PG quasars and EESBHs. In order to quantify this problem, here we find that $\mathcal{R} \cdot \lambda_{\mathrm{Edd}} = 1.3 \times 10^6 (L_{\mathrm{R}}/L_{\mathrm{Edd}})$ (being free of the parameter
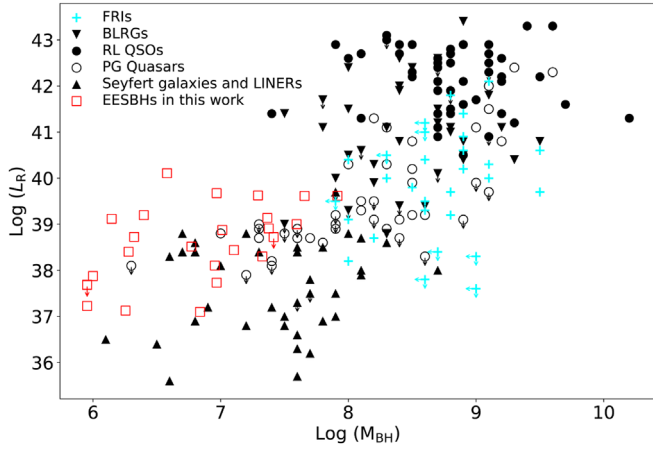
Figure 3. The 5 GHz core radio luminosity L_R vs. black hole mass M_{BH}. The markers are designated in the upper left corner.
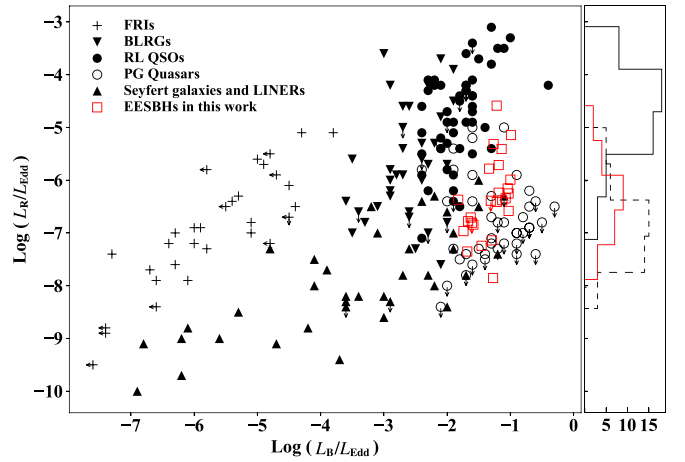

Figure 4. The 5 GHz core luminosity vs. the B-band luminosity, both in Eddington units. The markers are designated in the upper left corner. Right histogram: the black solid line histogram plots the distribution of L_R/L_{Edd} for the RL QSOs, the black dashed line histogram is for PG quasars, and the solid red line is for EESBHs in this work.

L_B); if there is no correlation between L_R and L_{Edd} or they are identical, then $\log \mathcal{R}$ versus $\log \lambda_{Edd}$ naturally has a slope of -1 caused by the mutual dependence on L_B and vice versa. We therefore explored the correlation between the 5 GHz core radio luminosity L_R and the Eddington luminosity L_{Edd}; here we use M_{BH} to replace L_{Edd} owing to the equation $L_{Edd} = 3.2 \times 10^4 (M_{BH}/M_\odot) L_\odot$ (see Figure 3). There is a clear linear correlation between L_R and M_{BH}, and the linear regression gives a slope of 4.86 ± 0.05 at a significance level of $>95\%$, which differs from 1, and for that reason the correlation between $\log \mathcal{R}$ and $\log \lambda_{Edd}$ is not caused by the mutual dependence on L_B.

Figure 4 shows the radio luminosity versus the optical luminosity expressed in Eddington units. There is no clear boundary between the sequence of radio-loud and radio-quiet sources in our plot compared to the results in Sikora et al. (2007). Our EESBHs are located in the high end of optical luminosity and have an intermediate distribution of radio luminosity that lies between the radio-loud quasar sample and the PG quasar sample (see the histogram in Figure 4).

6. Discussion

6.1. The Origin of Radio Emission: AGN or Star-forming Activity?

In the central kiloparsec region of the radio-quiet AGN host galaxies, the AGN is often not the only source producing the observed radio emission. Recalling that the radio emission from galaxies may have various origins in Section 1, e.g., from stellar activities such as thermal free–free emission from HII regions (e.g., Lacey et al. 1997; Ulvestad & Antonucci 1997), nonthermal synchrotron radio emission (Lisenfeld & Völk 2000) from young supernovae (SNe; e.g., Kronberg & Sramek 1985, 1992; Colina et al. 2001; Alberdi et al. 2006) and supernova remnants (e.g., Muxlow et al. 1994; Ulvestad & Antonucci 1997), or from the jets of AGNs (see Ho 2008, and references therein). It is quite possible that the star-forming activities will dominate observed radio emission of the central kiloparsec region in starburst galaxies (e.g., Ulvestad & Antonucci 1997; Tarchi et al. 2000; Fenech et al. 2008; Batejat et al. 2011). Several observational characteristics can be used to discriminate between the radio emissions from AGNs and star-forming activities, such as the brightness temperature, the spectral index, and the radio morphology (see Panessa et al.

2019, and references therein). In the following sections, we explore the radio emission of our EESBHs by using these indicators.

6.1.1. Radio Morphology, Spectral Index, and Brightness Temperature

Previous studies show that an AGN is still the dominating radio-emitting source at radio flux densities above 0.1 mJy in radio-quiet AGNs (Padovani et al. 2011; Bonzini et al. 2013). This indicates that the radio emission in most of our EESBHs could be from AGN activities, and only three sources (J1431 +2817, J0107+1408, and J1140+0307) are below this threshold. In our EESBH sample, J2242+2943 (Akn 564) is the only source showing evident AGN activity with a collimated linear structure extending ~ 1 kpc toward the north and three resolved components in the VLA 5 GHz and 8.4 GHz images (see Figure 5). Furthermore, two sources (J1559+3501 and J2236+1343) show flat or inverted spectra, suggesting that the radio emission is from AGNs.

Our EESBHs show a moderate brightness temperature range of $T_B \sim 10^2$–10^5 K at both 5 and 8.4 GHz as compared to radio-loud AGNs. Only two sources (J1536+5433 and J1703 +4540) have radio brightness temperatures above 10^5 K, i.e., $10^{5.36}$ and $10^{5.10}$ K, respectively. Since a star-forming region cannot reach $T_B \sim 10^5$ K at frequency $\nu > 1$ GHz (Condon et al. 1991; Condon 1992), we conclude that the radio emission observed in these two sources is preferentially from AGN activities.

Additionally, eight sources have a radio brightness temperature $T_B \gtrsim 10^4$ K (but $<10^5$ K; see Column (9) of Table 3) at 5 and 8.4 GHz and would also imply nonthermal radio emission, because a star-forming region can rarely exceed 10^4 K at such high frequencies (Condon 1992). The highest brightness temperatures from star-forming regions have been observed in luminous and ultraluminous infrared galaxies (LIRGs and ULIRGs, respectively), which is 10^4–10^5 K (e.g., Condon et al. 1991; Pérez-Torres et al. 2009; Varenius et al. 2014). As none of these eight sources have been found to be LIRGs/ULIRGs, this strongly indicates the AGN-dominated radio emission (e.g., Ulvestad & Antonucci 1997). Indeed, among these eight objects, high radio brightness temperature nuclei ($T_B > 10^6$ K)
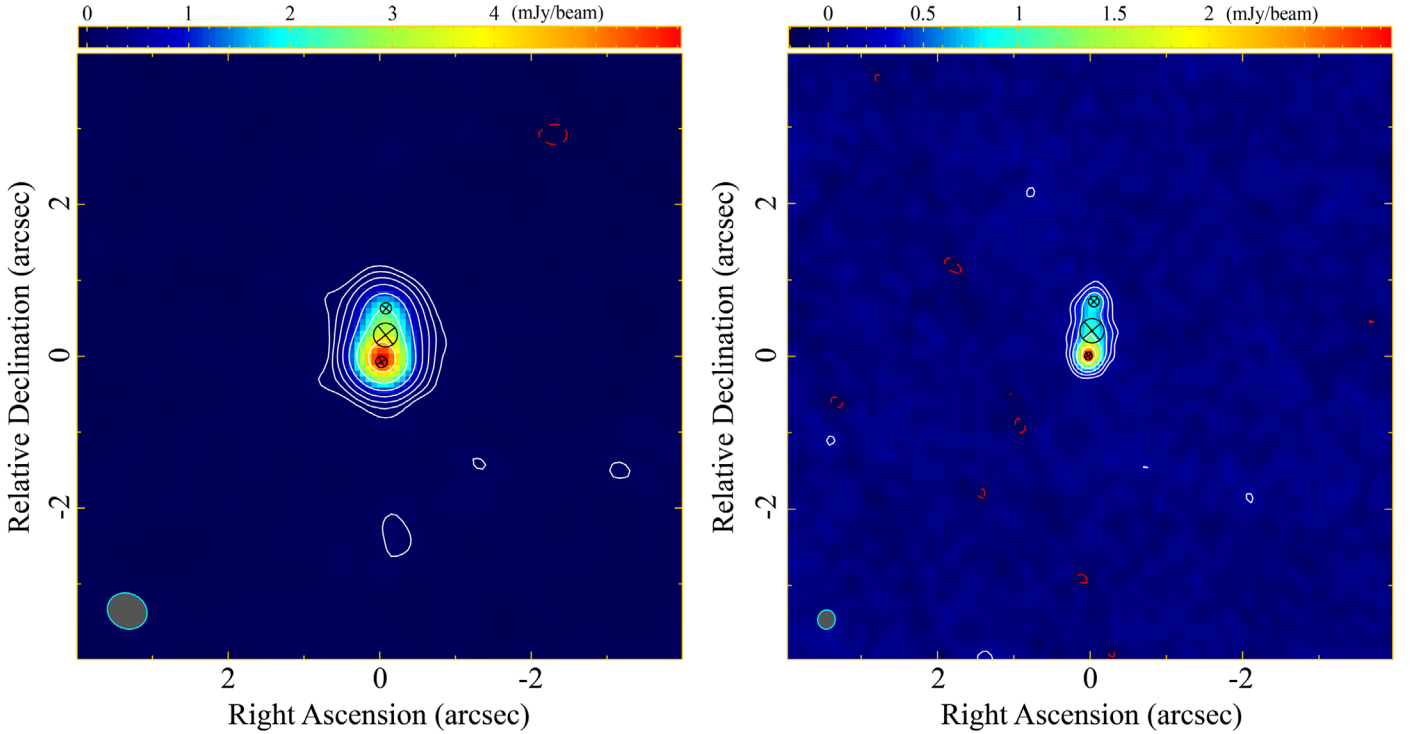
Figure 5. Natural-weighting VLA A-array images of J2242+2943 (Akn 564) at 5 GHz (left) and 8.4 GHz (right). Contours are drawn beginning at 3σ and increase by a factor of 2 thereafter. The rms noise is $\sigma_5 = 0.029$ mJy beam^{-1} and $\sigma_{8.5} = 0.044$ mJy beam^{-1}, respectively. The negative contours are plotted as red dashed lines, and positive ones are plotted as the solid white lines. The restoring beam is shown in the lower left corner of each panel. The FWHM of Gaussian model components is plotted as a black circle. The source is resolved into three components at C and X bands; we only take account of the integrated flux density of the central component, which is 5.84 ± 0.03 mJy at C band and 3.18 ± 0.07 mJy at X band. The size of the radio structure is $\sim 2''$ (corresponding to physical linear size of ~ 4 kpc).

have been detected for J0006+2012 (Mrk 335) and J0053 +1241 (IZw1) by our Very Long Baseline Array (VLBA) observations at 1.4 GHz (Obs. ID: BY145, in preparation) and for J2242+2943 (Akn 564; Lal et al. 2004).

We note that more than half of the our sample sources have a very low radio brightness temperature compared with an AGN. We have checked the infrared and far-infrared data and found that eight sources were detected by the Infrared Astronomical Satellite (IRAS). Among them, four sources (J0041+4021, J1405+2555, J1442+3526, and J1703+4540) have infrared and far-infrared luminosity $L_{\rm IR/FIR} > 10^{11} L_\odot$, i.e., the so-called type 1 (ultra)luminous infrared galaxies (e.g., Ulvestad & Antonucci 1997). Among these four objects, the radio emission from J1703+4540 (B3 1702+457) has already been proven to be from an AGN (Gu & Chen 2010). In contrast, the radio emission from the remaining sources is likely dominated by the star-forming activity. It should be emphasized here that the radio brightness temperature estimated in this paper is only the lower limit, constrained by the limited resolution of the VLA A-array. Therefore, high-resolution very long baseline interferometry (VLBI) observation is crucial to distinguish the various origins of the radio emission from radio-quiet AGNs. In this section, we can confirm that among 25 EESBHs, the radio emission from at least 11 sources is dominated by AGN activities.

6.1.2. Estimating Star Formation Rate Surface Density with Radio Emission

In order to further distinguish the radio emission from the star-forming activities and AGNs, we can compare the star formation rates (SFRs) measured by using direct indicators

with the radio emission estimates. Here we estimate the SFR requirements for the observed radio emission using the empirical relation derived by Condon (1992). It was proven in star-forming galaxies that the SFRs estimated with this relation are well consistent with those estimated from the infrared radiation (see, e.g., Rabidoux et al. 2014). Here we only estimate the SFRs from the nonthermal process since there are higher SFR requirements for thermal processes than nonthermal to produce equal radio luminosity. This will give us the lowest SFR requirement in producing the observed radio emission. The formula is

$$\left(\frac{L_N}{\rm W\ Hz^{-1}}\right) \sim 5.3 \times 10^{21} \left(\frac{\nu}{\rm GHz}\right)^{-0.8} \left(\frac{\rm SFR_N(M \geqslant 5\ M_\odot)}{M_\odot\ \rm yr^{-1}}\right),$$

$$(3)$$

where L_N are the nonthermal radio luminosities and $\rm SFR_N(M \geqslant 5\ M_\odot)$ is the star formation rate of stars more massive than $5\ M_\odot$, estimated from the nonthermal process (i.e., nonthermal radio flux density). The extended Miller−Scalo initial mass function (Miller & Scalo 1979) with an exponent of -2.5 was used, and it was assumed that all stars with mass greater than $8\ M_\odot$ become SNe and that the dust absorption is negligible in deriving these formulae (Condon 1992). Here we assume a typical spectral index of $\alpha_N = -0.8$ for the nonthermal radio emission. The final $\rm SFR_N(M \geqslant 5\ M_\odot)$ is subsequently scaled to the total SFRs ($M \geqslant 0.1\ M_\odot$) by a scaling factor of 5.6 (Rabidoux et al. 2014). We calculated the disk-averaged surface densities of the SFRs ($\Sigma_{\rm SFR}$) by dividing the size of emission regions, derived from the major and minor axis of the synthesis beam.
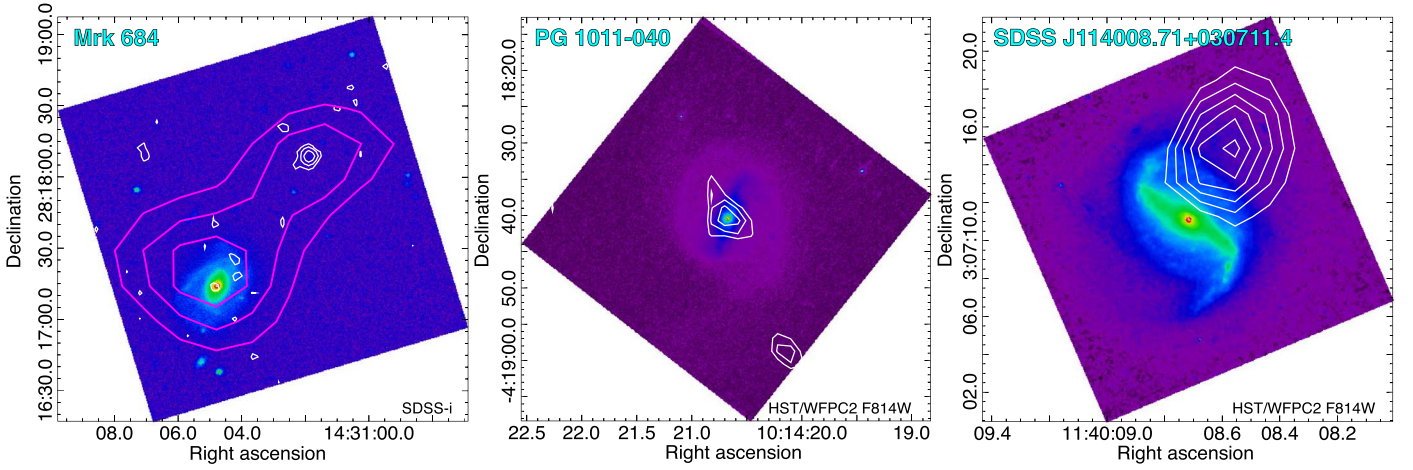
Figure 6. FIRST (white contours) and/or NVSS (pink contours) 1.4 GHz VLA images overlaid on the optical images (pseudo-color images). The markers for the optical images are at the lower right. The optical image for J1431+2817 (Mrk 684) is from the SDSS i band, and those for J1014−0418 (PG 1011−040) and J1140 +0307 (SDSS J114008.71+030711.4) are from HST/WFPC F814W. The contours are plotted as $(1, 2.25, 3.37, 5.06, ...) \times 3\sigma$.

The results are listed in the last column of Table 3. Most of our EESBHs (20 out of 25) have a lower limit for the SFR surface density $\Sigma_{\mathrm{SFR}} \gtrsim 10\, M_\odot\, \mathrm{yr}^{-1}\, \mathrm{kpc}^{-2}$ estimated at 5 GHz or 8.4 GHz. Among 20 sources, 10 have $\Sigma_{\mathrm{SFR}} \gtrsim 100\, M_\odot\, \mathrm{yr}^{-1}\, \mathrm{kpc}^{-2}$. It was noted that NLS1s tend to have a high fraction of circumnuclear star-forming rings at more or less than 1 kpc from the core (Deo et al. 2006; Hennig et al. 2018), while it is still very difficult to reach a star formation surface density of $10\, M_\odot\, \mathrm{yr}^{-1}\, \mathrm{kpc}^{-2}$ (see Kormendy & Kennicutt 2004; Kennicutt & Evans 2012). Five objects in our sample have the lowest requirement of $\Sigma_{\mathrm{SFR}} < 10\, M_\odot\, \mathrm{yr}^{-1}\, \mathrm{kpc}^{-2}$ in producing the observed radio emission: J0107+1408, J1118+4025, J1140+0307, J1153 +4612, and J1431+2817. J1153+4612 and J1431+2817 have a far-infrared luminosity $L_{\mathrm{FIR}} \sim 10^{10}\, L_\odot$, suggesting a high SFR on the scale of the whole galaxy, which does not result in a high SFR surface density. Particularly, J1153+4612 (Mrk 42) was found to have a starburst ring at ~ 300 pc (Muñoz Marín et al. 2007) and have a total ring SFR of $1.38\, M_\odot\, \mathrm{yr}^{-1}$ (Hennig et al. 2018), which is still below the lower limit required to produce the observed radio emission. Moreover, the VLA A-array has a resolution of ~ 200 pc at C band for Mrk 42, which suggests that the radio emission from J1153+4612 (Mrk 42) is less likely to result from the star-forming activity. We should note here that the SFR surface density required to produce the observed radio emission will be even larger than the value given here if we take thermal fractions into account and use the intrinsic size of the emission regions. Thus, we conclude that the radio emission from most of our EESBHs (at least 21 out of 25) is from AGN activities; otherwise, strong nuclear star formation is required to give the observed radio emission.

6.2. AGNs with Super-Eddington Accretion Rates: Comparing with XRBs

With the population of EESBHs, as presented in this paper, we found that super-Eddington accreting AGNs have a low radio luminosity ($L_5 \sim 10^{38}\, \mathrm{erg\, s^{-1}}$) and most of them ($\gtrsim$90%) are radio-quiet ($\mathcal{R} \lesssim 10$). There is only one super-Eddington source (J1034+3938) in our sample marginally located in the radio-loud region ($\mathcal{R} = 12$). This confirms the radio quiescence when Eddington ratios approach or exceed 1. More

generally, there is an inverse correlation between radio-loudness and the Eddington ratio from the sub-Eddington to the super-Eddington regime. In this work, we have extended the inverse $\mathcal{R} - \lambda_{\mathrm{Edd}}$ correlation to the super-Eddington regime (see Figure 2), supporting a continuous jet suppression with an increasing Eddington ratio as proposed by Ho (2002) when overcoming the Eddington limit.

AGNs with extremely high Eddington ratios and Galactic accreting black holes in a very high state (e.g., Greene et al. 2006) hold the same tendency of the radio-loudness versus the Eddington ratio (e.g., Broderick & Fender 2011). Furthermore, with the state transition in XRBs from the low/hard state to the high/soft state, a radio outburst is always associated with the soft X-ray peak at the end of the transition phase, i.e., the very high state. Some of our extremely high Eddington accreting AGNs indeed show kiloparsec-scale emission or kiloparsec-scale radio structures (KSRs) in their FIRST and NVSS images, implying a past ejecting activity. The kiloparsec-scale radio emission in J1703+4540 (B3 1702+457) was already noted by Giroletti et al. (2017). J1431+2817 (Mrk 684) shows an extension of ~ 60 kpc to the northwest in the NVSS 1.4 GHz image (left panel of Figure 6). The NVSS image reveals a two-component system, where the second component is consistent in position with FIRST. A visual inspection of the SDSS-i image confirms that there is no obvious optical counterpart associated with the second component that also shows a structure of an AGN hotspot, implying a physical connection with the radio nucleus. J1014−0418 (PG 1011−040) shows a slight bipolar extension in the FIRST image toward the northeast and the southwest, perpendicular to the major axis of the host galaxy (middle panel of Figure 6). These characteristics more likely imply that the central AGN is responsible for this radio emission (e.g., Yang et al. 2019), whereas a strong starburst nucleus is also possible (e.g., Seaquist & Odegard 1991). In J1140+0307 (SDSS J114008.71 +030711.4), we find a strong radio source offset northwest from the galaxy center in the FIRST 1.4 GHz image at a distance of $4\rlap{.}''5$ (7 kpc) with a peak flux density of 0.84 ± 0.15 mJy (see Figure 6). There is no optical counterpart coinciding with this radio source in the HST/WFPC2 F814W image, implying that the central AGN or an off-nuclear massive black hole (see Reines et al. 2020) is responsible for this

emission. Previous studies showed that kiloparsec-scale radio structures might be a common feature in radio-loud Seyfert galaxies. About 10 NLS1s so far show kiloparsec-scale radio structures, including one radio-quiet source (Gliozzi et al. 2010; Doi et al. 2012, 2015; Richards & Lister 2015). If AGNs have a similar state transition to XRBs, then the kiloparsec-scale radio structures found in our sample might imply the past ejecting activities during the transition state. Similarly, the Galactic X-ray binary SS 433 has super-Eddington ratio accretion at all times during the outbursts, and the episodes of jet activity are responsible for the formation and shaping of the surrounding elongated radio structures (e.g., Broderick et al. 2018).

The very high state in Galactic black holes possesses the highest Eddington ratio but is not super-Eddington. It was suggested that super-Eddington accretion in ULXs and some XRBs might indicate a new "ultraluminous" accretion state (Gladstone et al. 2009; Sutton et al. 2013; Brorby et al. 2015; Roberts et al. 2016), which is supported by the finding of a few microquasars with super-Eddington accretion that can transit between classical states and the ultraluminous state (e.g., GRS 1915+105; see Fender et al. 2004). The same scenario was also proposed to explain the powerful radio-emitting outflows in tidal disruption events (e.g., Giannios & Metzger 2011). In the future, studies of time-domain radio properties in super-Eddington accreting AGNs may help to test the analogy with stellar-mass accreting systems in the ultraluminous state.

6.3. The Origin of Radio Emission: Jet-driven versus Outflow-driven and Corona-driven

The extremely high Eddington ratio accreting AGNs are predominately radio-quiet, whereas the radio emission is not completely absent or is dramatically reduced in comparison with the sub-Eddington ratio AGNs (see Figure 2). In radio-quiet AGNs, several radio-emitting mechanisms are still in competition with each other, such as low-power jets, radio-emitting wind-like outflows, and magnetized corona/jet base. In this paragraph, we will further discuss the origin of radio emission among several AGN-dominated activities.

We have explored the correlation between the radio and X-ray luminosities and between the radio spectral index and the Eddington ratio. Figure 7 shows the radio luminosity versus the X-ray luminosity with markings of the $\log L_R/L_X = -5$ and $\log L_R/L_X = -4$ lines. Most of our extremely high Eddington accreting AGNs have a radio-to-X-ray luminosity ratio in the range $\log L_R/L_X = -5$ to -4. Sources with a radio-to-X-ray luminosity ratio $\log L_R/L_X \sim -5$ are found to be similar to coronally active stars, which would imply magnetized corona/jet base dominated radio emission. Because the radio emission from radio-loud AGNs, and hence from jets, has a radio-to-X-ray luminosity ratio of $\log L_R/L_X \sim 10^{-2}$ to 1, sources having a radio-to-X-ray luminosity ratio close to or slightly exceeding $\log L_R/L_X \sim -4$ would imply a combination of corona and jets (Laor & Behar 2008; Behar et al. 2015; Laor et al. 2019).

Figure 8 shows the distribution of the nonsimultaneous radio spectral index α along the Eddington ratio λ_{Edd}; the spectral index uncertainties are estimated from the integrated flux density errors. The nonsimultaneity of the 1.4, 5, and 8.4 GHz observations in these objects may induce spectral index errors, whereas it may not lead to a large uncertainty in spectral index owing to the stability of radio emission of our EESBHs (see
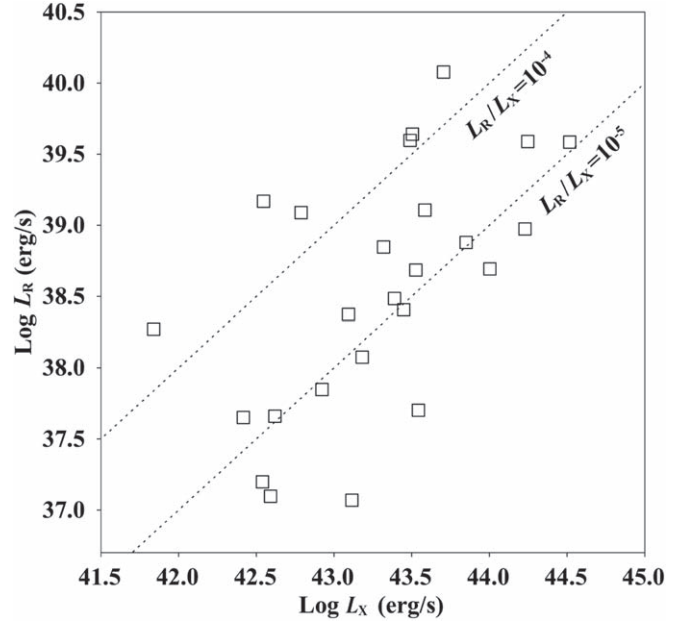

Figure 7. The 5 GHz radio luminosity vs. the 2–10 keV X-ray luminosity for our EESBH sources. The gray dashed lines correspond to $L_R/L_X = 10^{-5}$ and $L_R/L_X = 10^{-4}$.
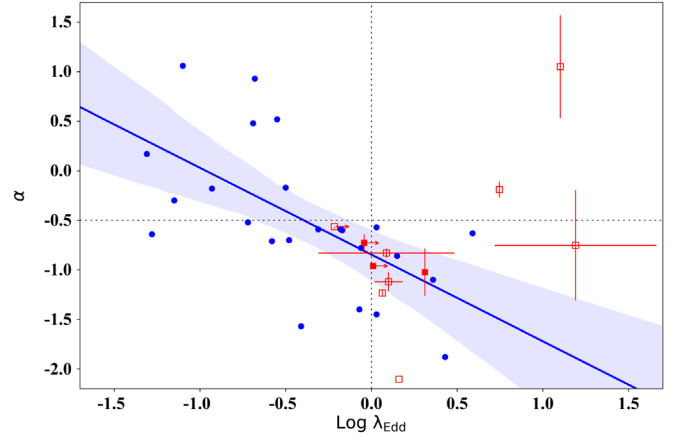

Figure 8. Radio spectral index α vs. Eddington ratio λ_{Edd}. The spectral index is measured between 1.4 and 5 GHz (red filled squares) and between 5 and 8.5 GHz (red open squares) for our EESBHs. The 5–8.4 GHz spectral index and the Eddington ratio distribution for radio-quiet quasars from Laor et al. (2019) are plotted as blue circles, where the blue line and belt are the linear regression and 95% confidence interval, respectively. The horizontal dotted line at $\alpha = -0.5$ is the division of flat (above) and steep (below) spectrum radio sources, and the vertical dotted line designates $\lambda_{Edd} = 1$.

Section 4). Most (9 out of 11) of our sources have a steep radio spectrum, implying that the ejecta rather than the core dominates the radio emission from our EESBHs. In Figure 8, we also plot the 5–8.4 GHz spectral index and the Eddington ratio distribution for radio-quiet quasars from Laor et al. (2019) as a comparison. Laor et al. (2019) discovered an inverse correlation between α and λ_{Edd} using a sample of 25 radio-quiet quasars, spanning a large range of $\log \lambda_{Edd}$ from -1.6 to 0.6. Note that the high-Eddington ($\log \lambda_{Edd} > -0.5$) quasars tend to have a steep spectrum ($\alpha < -0.5$, i.e., below the horizontal dotted line in Figure 8), and it was interpreted as that the radio emission is from optically thin outflows (see Laor et al. 2019). It is clear from Figure 8 that most of our high-Eddington sources follow a similar trend. Furthermore, the 11

EESBHs have a radio-to-X-ray luminosity ratio of $\log L_R/L_X \sim -5$, suggesting a contribution from the radio-emitting corona (Laor & Behar 2008; Behar et al. 2015; Laor et al. 2019). To sum up, a possible interpretation for the radio emission in our EESBHs is the transient ejecta caused by the optically thin outflow (outflowing corona), which enhances the comparison between the high-Eddington AGNs and XRBs in the soft state since the transient ejections were generally observed in the soft state of XRBs.

Interestingly, few of our highly super-Eddington systems with $\log \lambda_{\rm Edd} \gtrsim 0.6$ do not follow the above trend (see Figure 8). The flatter radio spectra in such cases might be likely due to the jet activity. However, the observed radio-to-X-ray luminosity ratio for the three highly super-Eddington ratio AGNs is $L_R/L_X \lesssim 10^{-5}$, which rules out the possibility of traditional ("BP" or "BZ") jets (e.g., Blandford & Znajek 1977; Blandford & Payne 1982), and the radio emission is suggested to be dominated by a magnetized corona (aka jet base). The other possibility is that the radiation-pressure-driven jets start to dominate in this regime (e.g., Takeuchi et al. 2009; Fabrika et al. 2015; Sádowski & Narayan 2015), where a weak and short jet produces optically thick radio emission and appears like a scaled-down version of radio-loud AGNs. Interestingly, there is a slight positive $\alpha - \lambda_{\rm Edd}$ correlation that has been found in radio-loud quasars (see Laor et al. 2019), which may likely support this idea. Extended radio emission was observed in the Galactic microquasar SS 433, which was attributed to a mixture of radiation-pressure-driven jets and radio-emitting outflow (e.g., Okuda et al. 2005). There is only one source (J2242 +2943 or Akn 564) in our sample that shows such quasi-continuous radio ejection, and VLBA images show that J1703 +4540 (B3 1702+457) in our EESBH sample has a bipolar emission (Doi et al. 2011). More such super-Eddington accreting AGNs with simultaneous multiband observations are required to confirm these spectral characteristics. Furthermore, future VLBI observation of super-Eddington accreting AGNs will provide more evidence on the different radio-emitting mechanisms proposed here.

7. Summary

The main results of this paper are summarized as follows:

1. The compact and core-dominated radio emission is found in our sample of EESBHs. Most of the radio emission originates within the central few hundred parsecs to 1 kpc region, implying that the sources are compact at these scales.

2. In our extremely high Eddington accreting systems, we have estimated the lowest SFR surface density required to produce the observed radio emission. This surface density is higher than the maximum value that has been detected in circumnuclear starburst galaxies, suggesting that the radio emission comes from AGN activity.

3. A global inverse correlation has been established between the radio-loudness $\mathcal{R}$ and the Eddington ratio $\lambda_{\rm Edd}$ from the sub- to the super-Eddington regime. There is no clear demarcation found in this distribution for EESBHs, indicating a continuous suppression of radio emission from the high- to the super-Eddington regime. Super-Eddington accreting AGNs are predominately radio-quiet, but not completely radio quenched.

4. The high-Eddington and mildly super-Eddington AGNs ($-0.5 < \log \lambda_{\rm Edd} < 0.6$) have a radio-to-X-ray luminosity ratio $L_R/L_X \sim 10^{-5} - 10^{-4}$ and a steep radio spectrum, implying that the radio emission was dominated by the transient ejecta, where the outflowing corona may be at work.

ORCID iDs

Xiaolong Yang ⓘ https://orcid.org/0000-0002-4439-5580
Su Yao ⓘ https://orcid.org/0000-0002-9728-1552
Luis C. Ho ⓘ https://orcid.org/0000-0001-6947-5846
Tao An ⓘ https://orcid.org/0000-0003-4341-0029
Ran Wang ⓘ https://orcid.org/0000-0003-4956-5742
Willem A. Baan ⓘ https://orcid.org/0000-0003-3389-6838
Minfeng Gu ⓘ https://orcid.org/0000-0002-4455-6946
Ravi Joshi ⓘ https://orcid.org/0000-0002-5535-4186

References

Abdo, A. A., Ackermann, M., Ajello, M., et al. 2009, ApJL, 707, L142
Abramowicz, M. A., Czerny, B., Lasota, J. P., & Szuszkiewicz, E. 1988, ApJ, 332, 646
Alberdi, A., Colina, L., Torrelles, J. M., et al. 2006, ApJ, 638, 938
Auchettl, K., Guillochon, J., & Ramirez-Ruiz, E. 2017, ApJ, 838, 149
Batejat, F., Conway, J. E., Hurley, R., et al. 2011, ApJ, 740, 95
Becker, R. H., White, R. L., & Helfand, D. J. 1995, ApJ, 450, 559
Begelman, M. C., King, A. R., & Pringle, J. E. 2006, MNRAS, 370, 399
Begelman, M. C., & Volonteri, M. 2017, MNRAS, 464, 1102
Behar, E., Baldi, R. D., Laor, A., et al. 2015, MNRAS, 451, 517
Behar, E., Vogel, S., Baldi, R. D., Smith, K. L., & Mushotzky, R. F. 2018, MNRAS, 478, 399
Berger, E., Zauderer, A., Pooley, G. G., et al. 2012, ApJ, 748, 36
Berton, M., Congiu, E., Järvelä, E., et al. 2018, A&A, 614, A87
Blandford, R. D., & Payne, D. G. 1982, MNRAS, 199, 883
Blandford, R. D., & Znajek, R. L. 1977, MNRAS, 179, 433
Bloom, J. S., Giannios, D., Metzger, B. D., et al. 2011, Sci, 333, 203
Blundell, K. M., Mioduszewski, A. J., Muxlow, T. W. B., Podsiadlowski, P., & Rupen, M. P. 2001, ApJL, 562, L79
Bonzini, M., Padovani, P., Mainieri, V., et al. 2013, MNRAS, 436, 3759
Boroson, T. A., & Green, R. F. 1992, ApJS, 80, 109
Brightman, M., Silverman, J. D., Mainieri, V., et al. 2013, MNRAS, 433, 2485
Broderick, J. W., & Fender, R. P. 2011, MNRAS, 417, 184
Broderick, J. W., Fender, R. P., Miller-Jones, J. C. A., et al. 2018, MNRAS, 475, 5360
Brorby, M., Kaaret, P., & Feng, H. 2015, MNRAS, 448, 3374
Burrows, D. N., Kennea, J. A., Ghisellini, G., et al. 2011, Natur, 476, 421

Castelló-Mor, N., Netzer, H., & Kaspi, S. 2016, MNRAS, 458, 1839
Colina, L., Alberdi, A., Torrelles, J. M., Panagia, N., & Wilson, A. S. 2001, ApJ, 553, L19
Condon, J. J. 1992, ARA&A, 30, 575
Condon, J. J., Cotton, W. D., Greisen, E. W., et al. 1998, AJ, 115, 1693
Condon, J. J., Huang, Z. P., Yin, Q. F., & Thuan, T. X. 1991, ApJ, 378, 65
Czerny, B., Wang, J.-M., Du, P., et al. 2019, ApJ, 870, 84
Dai, L., McKinney, J. C., Roth, N., Ramirez-Ruiz, E., & Miller, M. C. 2018, ApJL, 859, L20
Deo, R. P., Crenshaw, D. M., & Kraemer, S. B. 2006, AJ, 132, 321
Doi, A., Asada, K., Fujisawa, K., et al. 2013, ApJ, 765, 69
Doi, A., Asada, K., & Nagai, H. 2011, ApJ, 738, 126
Doi, A., Nagira, H., Kawakatu, N., et al. 2012, ApJ, 760, 41
Doi, A., Wajima, K., Hagiwara, Y., & Inoue, M. 2015, ApJL, 798, L30
Dotan, C., & Shaviv, N. J. 2011, MNRAS, 413, 1623
Du, P., Hu, C., Lu, K.-X., et al. 2015, ApJ, 806, 22
Fabrika, S., Ueda, Y., Vinokurov, A., Sholukhova, O., & Shidatsu, M. 2015, NatPh, 11, 551
Falcke, H., Körding, E., & Markoff, S. 2004, A&A, 414, 895
Fender, R., Corbel, S., Tzioumis, T., et al. 1999, ApJ, 519, L165
Fender, R. P., Belloni, T. M., & Gallo, E. 2004, MNRAS, 355, 1105
Fenech, D. M., Muxlow, T. W. B., Beswick, R. J., Pedlar, A., & Argo, M. K. 2008, MNRAS, 391, 1384
Giannios, D., & Metzger, B. D. 2011, MNRAS, 416, 2102
Gies, D. R., McSwain, M. V., Riddle, R. L., et al. 2002, ApJ, 566, 1069
Giroletti, M., & Panessa, F. 2009, ApJL, 706, L260
Giroletti, M., Panessa, F., Longinotti, A. L., et al. 2017, A&A, 600, A87
Gladstone, J. C., Roberts, T. P., & Done, C. 2009, MNRAS, 397, 1836
Gliozzi, M., Papadakis, I. E., Grupe, D., et al. 2010, ApJ, 717, 1243
Greene, J. E., Ho, L. C., & Ulvestad, J. S. 2006, ApJ, 636, 56
Greiner, J., Cuby, J. G., & McCaughrean, M. J. 2001, Natur, 414, 522
Gu, M., & Chen, Y. 2010, AJ, 139, 2612
Gültekin, K., Cackett, E. M., King, A. L., Miller, J. M., & Pinkney, J. 2014, ApJL, 788, L22
Haardt, F., & Maraschi, L. 1991, ApJL, 380, L51
Hada, K., Doi, A., Wajima, K., et al. 2018, ApJ, 860, 141
Hennig, M. G., Riffel, R. A., Dors, O. L., et al. 2018, MNRAS, 477, 1086
Ho, L. C. 2002, ApJ, 564, 120
Ho, L. C. 2008, ARA&A, 46, 475
Hopkins, A. M., Afonso, J., Chan, B., et al. 2003, AJ, 125, 465
Hovatta, T., Lister, M. L., Aller, M. F., et al. 2012, AJ, 144, 105
Inoue, Y., & Doi, A. 2018, ApJ, 869, 114
Jiang, Y.-F., Stone, J., & Davis, S. W. 2019, ApJ, 880, 67
Jin, C., Done, C., Ward, M., & Gardner, E. 2017, MNRAS, 471, 706
Jin, C., Ward, M., & Done, C. 2012a, MNRAS, 425, 907
Jin, C., Ward, M., Done, C., & Gelbord, J. 2012b, MNRAS, 420, 1825
Kaaret, P., Feng, H., & Roberts, T. P. 2017, ARA&A, 55, 303
Kellerman, K. I., Sramek, R., Schmidt, M., Shaffer, D. B., & Green, R. 1989, AJ, 98, 1195
Kelley, L. Z., Tchekhovskoy, A., & Narayan, R. 2014, MNRAS, 445, 3919
Kennicutt, R. C., & Evans, N. J. 2012, ARA&A, 50, 531
Kinney, A. L., Schmitt, H. R., Clarke, C. J., et al. 2000, ApJ, 537, 152
Körding, E. G., Jester, S., & Fender, R. 2006, MNRAS, 372, 1366
Kormendy, J., & Ho, L. C. 2013, ARA&A, 51, 511
Kormendy, J., & Kennicutt, R. C. J. 2004, ARA&A, 42, 603
Kronberg, P. P., & Sramek, R. A. 1985, Sci, 227, 28
Kronberg, P. P., & Sramek, R. A. 1992, in X-ray Emission from Active Galactic Nuclei and the Cosmic X-ray Background, ed. W. Brinkmann & J. Trumper (Garching: Max-Planck-Institut fur Extraterrestrische Physik), 247
Kuźmicz, A., Jamrozy, M., Bronarska, K., Janda-Boczar, K., & Saikia, D. J. 2018, ApJS, 238, 9
Lacey, C., Duric, N., & Goss, W. M. 1997, ApJS, 109, 417
Lal, D. V., Shastri, P., & Gabuzda, D. C. 2004, A&A, 425, 99
Lanzuisi, G., Perna, M., Comastri, A., et al. 2016, A&A, 590, A77

Laor, A., Baldi, R. D., & Behar, E. 2019, MNRAS, 482, 5513
Laor, A., & Behar, E. 2008, MNRAS, 390, 847
Levan, A. J., Tanvir, N. R., Cenko, S. B., et al. 2011, Sci, 333, 199
Lietzen, H., Heinämäki, P., Nurmi, P., et al. 2011, A&A, 535, A21
Lisenfeld, U., & Völk, H. J. 2000, A&A, 354, 423
Lu, Y., & Yu, Q. 1999, ApJL, 526, L5
Marconi, A., Risaliti, G., Gilli, R., et al. 2004, MNRAS, 351, 169
Martínez-Paredes, M., Aretxaga, I., Alonso-Herrero, A., et al. 2017, MNRAS, 468, 2
McKinney, J. C., Dai, L., & Avara, M. J. 2015, MNRAS, 454, L6
McLure, R. J., & Dunlop, J. S. 2004, MNRAS, 352, 1390
McMullin, J. P., Waters, B., Schiebel, D., Young, W., & Golap, K. 2007, adass, 376, 127
Meier, D. 1996, ApJ, 459, 185
Merloni, A., Heinz, S., & di Matteo, T. 2003, MNRAS, 345, 1057
Middleton, M. J., Walton, D. J., Alston, W., et al. 2018, arXiv:1810.10518
Miller, G. E., & Scalo, J. M. 1979, ApJS, 41, 513
Mirabel, I. F., & Rodríguez, L. F. 1994, Natur, 371, 46
Muñoz Marín, V. M., González Delgado, R. M., Schmitt, H. R., et al. 2007, AJ, 134, 648
Muxlow, T. W. B., Pedlar, A., Wilkinson, P. N., et al. 1994, MNRAS, 266, 455
Narayan, R., Igumenshchev, I. V., & Abramowicz, M. A. 2003, PASJ, 55, L69
Neilsen, J., & Lee, J. C. 2009, Natur, 458, 481
Ohsuga, K., & Mineshige, S. 2011, ApJ, 736, 2
Okuda, T., Teresi, V., Toscano, E., & Molteni, D. 2005, MNRAS, 357, 295
Osterbrock, D. E., & Pogge, R. W. 1985, ApJ, 297, 166
Padovani, P., Miller, N., Kellermann, K. I., et al. 2011, ApJ, 740, 20
Panessa, F., Baldi, R. D., Laor, A., et al. 2019, NatAs, 3, 387
Pérez-Torres, M. A., Romero-Cañizales, C., Alberdi, A., & Polatidis, A. 2009, A&A, 507, L17
Perley, R. A., & Butler, B. J. 2013, ApJS, 204, 19
Rabidoux, K., Pisano, D. J., Kepley, A. A., Johnson, K. E., & Balser, D. S. 2014, ApJ, 780, 19
Raginski, I., & Laor, A. 2016, MNRAS, 459, 2082
Reines, A. E., Condon, J. J., Darling, J., & Greene, J. E. 2020, ApJ, 888, 36
Ricci, C., Paltani, S., Ueda, Y., & Awaki, H. 2013, MNRAS, 435, 1840
Richards, J. L., & Lister, M. L. 2015, ApJL, 800, L8
Roberts, T. P., Middleton, M. J., Sutton, A. D., et al. 2016, AN, 337, 534
Runnoe, J. C., Brotherton, M. S., & Shang, Z. 2012, MNRAS, 426, 2677
Schawinski, K., Koss, M., Berney, S., & Sartori, L. F. 2015, MNRAS, 451, 2517
Schmitt, H. R., Ulvestad, J. S., Antonucci, R. R. J., & Kinney, A. L. 2001, ApJS, 132, 199
Seaquist, E. R., & Odegard, N. 1991, ApJ, 369, 320
Shepherd, M. C., Pearson, T. J., & Taylor, G. B. 1994, BAAS, 26, 987
Sikora, M., Stawarz, Ł., & Lasota, J.-P. 2007, ApJ, 658, 815
Sądowski, A., & Narayan, R. 2015, MNRAS, 453, 3213
Sutton, A. D., Roberts, T. P., & Middleton, M. J. 2013, MNRAS, 435, 1758
Takeo, E., Inayoshi, K., Ohsuga, K., Takahashi, H. R., & Mineshige, S. 2018, MNRAS, 476, 673
Takeuchi, S., Mineshige, S., & Ohsuga, K. 2009, PASJ, 61, 783
Tarchi, A., Neininger, N., Greve, A., et al. 2000, A&A, 358, 95
Ulvestad, J. S., & Antonucci, R. R. J. 1997, ApJ, 488, 621
Ulvestad, J. S., Antonucci, R. R. J., & Barvainis, R. 2005, ApJ, 621, 123
Ulvestad, J. S., Antonucci, R. R. J., & Goodrich, R. W. 1995, AJ, 109, 81
Varenius, E., Conway, J. E., Martí-Vidal, I., et al. 2014, A&A, 566, A15
Vasudevan, R. V., & Fabian, A. C. 2007, MNRAS, 381, 1235
Volonteri, M., & Rees, M. J. 2005, ApJ, 633, 624
Volonteri, M., Silk, J., & Dubus, G. 2015, ApJ, 804, 148
Wang, J.-M., Du, P., Valls-Gabaud, D., Hu, C., & Netzer, H. 2013, PhRvL, 110, 081301
Wu, S., Coughlin, E. R., & Nixon, C. 2018, MNRAS, 478, 3016
Yang, J., An, T., Zheng, F., et al. 2019, MNRAS, 482, 1701
Zauderer, B. A., Berger, E., Soderberg, A. M., et al. 2011, Natur, 476, 425
Zhou, H., Wang, T., Yuan, W., et al. 2007, ApJL, 658, L13